FERMILAB-TM-2252
8 June 2004

The lead-glass electromagnetic calorimeter for the SELEX experiment

M. Y. Balatz [a,1], P. S. Cooper [b,2], G. V. Davidenko [a], A. G. Dolgolenko [a], G. B. Dzyubenko [a], A. V. Evdokimov [a,3], I. Giller [c], Y. M. Goncharenko [d], A. D. Kamenskii [a], M. A. Kubantsev [a,4], V. F. Kurshetsov [d], J. Lach [b], L. G. Landsberg [d], I. F. Larin [a], V. A. Matveev [a], M. A. Moinester [c], S. B. Nurushev [d], A. Ocherashvili [c], J. Russ [e,2], V. K. Semyatchkin [a], A. I. Sitnikov [a], V. Steiner [c], I. I. Tsukerman [a], A. N. Vasiliev [d], D. V. Vavilov [d], V. S. Verebryusov [a], V. A. Victorov [d], V. E. Vishnyakov [a].

[a] *Institute of Theoretical and Experimental Physics, Moscow, Russia*
[b] *Fermilab, Batavia, Illinois, U.S.A.*
[c] *Tel-Aviv University, 69978 Ramat Aviv, Israel*
[d] *Institute for High Energy Physics, Protvino, Russia*
[e] *Carnegie-Mellon Univ. Pittsburgh, Pennsylvania, U.S.A.*

Abstract

A large-acceptance, highly segmented electromagnetic lead glass calorimeter for Experiment E781 (*SELEX*) at Fermi National Acceleration Laboratory was designed and built. This detector has been used to reconstruct photons and electrons with energies ranging from few GeV up to 500 GeV in the collisions of the 650 GeV Σ^- hyperons and π^- mesons with the target nucleons. The design, calibration and performance of the calorimeter are described. Energy resolution and position resolution are assessed using both calibration electron beams and π^0 mesons reconstructed in 650 GeV hadron-hadron interactions. The performance of the calorimeter in selecting resonant states that involve photons is demonstrated.

Key words: calorimeter, lead-glass, radiation damage

1 Introduction

During the last decade there has been significant progress in the understanding of charm hadroproduction [1]. Several results from Fermilab and CERN fixed target programs established the short lifetime of the Λ_c^+ baryon, confirmed the difference in D_s^+ production from Σ and K beams, and confirmed the existence of the Ξ_c^+ baryon. From both hadronic experiments and e^+e^- annihilation data emerged new evidence of Σ_c^{++} and Σ_c^0. However, in comparison with the meson sector, the baryons are still largely unexplored. An international collaboration of the Fermilab experiment *E781* constructed a *SEgmented LargE X_f baryon spectrometer (SELEX)* to study the properties of charmed baryons produced in the hyperon beam of the Tevatron [2]. In the *SELEX* experiment, secondary particles are fully identified over the whole momentum range of interest for large-x_f charmed baryons. Particular attention has been given to weak decays of their ground states, like $\Lambda_c^+ \rightarrow \Lambda^0 \pi^+\pi^0$, to radiative and strong transitions like $\Xi_c^* \rightarrow \Xi_c + \gamma, \pi^0$ and to semileptonic decays of charmed mesons. The *SELEX* program also includes several non-charm physics topics like Coulomb production reactions with photons in the final state.

The electromagnetic calorimeter is based on total absorption Cherenkov counters with radiators of lead glass. It measures final state electrons and photons. Previous publications [3,4] described the prototypes of this detector. This paper focuses on the design, construction and performance of the Photon calorimeter.

Following a brief review of the *SELEX* spectrometer as a whole in Section 2, design and construction of the Photon calorimeter are described in Section 3. Section 4 describes electronics for data collection, readout and triggering. Section 5 of this paper deals with the design of the Photon calorimeter monitoring system. Section 6 describes magnetic shielding test results. In Section 7, energy calibration of the calorimeter is described. In Section 8, the performance of the gain monitoring system during the data-taking period is presented. Finally, Section 9 addresses the general performance of the Photon calorimeter during physics runs at the Tevatron accelerator. The results are summarized in Section 10.

---

[1] deceased

[2] E781 spokesman

[3] Corresponding author: Tel + 7 095 129 9438; e-mail: *evdokimo@itep.ru*

[4] Now at Northwestern University, Evanston, IL, USA

2 *SELEX* Setup

The general layout of the *SELEX* experiment is shown in Fig. 1. The *SELEX* spectrometer is a 60 m long, 3 stage spectrometer. The Fermilab Proton Center hyperon facility provides a variety of beams, which are brought to the *SELEX* spectrometer. The 650 GeV/c negative beam consists of about 50% Σ^- and 50% π^- at 10 m downstream of the hyperon production target [5]. The beam spectrometer, placed in front of the charm target, is equipped with silicon microstrip detectors to track incoming particles. There are two systems with different time selectivity - Beam HSD(100 ns) and BSSD(5 μs), where the latter is mounted on a monument block inside a noise shielded cage (RF-cage) together with the target followed by the vertex spectrometer formed by silicon microstrip detectors VSSD. Incoming particles are identified by a beam transition radiation detector (BTRD). At the end of the vertex spectrometer, Vertex HSD is mounted to RF-cage.

The ensemble of charm targets includes C, Si, Cu. In addition, *SELEX* has an independent 3% interaction length Pb target for Primakoff reactions, located 1 m upstream the charm targets (not shown).

The first dipole magnet is normally operated at 1.347 T, equivalent to a p_t kick of 0.74 GeV/c. The M1 spectrometer is designed to analyze particles in the 2.5 –15 GeV/c range. The tracking devices in this spectrometer consist of three proportional wire chambers M1 PWC, two drift chambers M1 DC, and two stations of silicon microstrip detectors (called Large Area Silicon Detectors, LASD1 and LASD2). A lead glass calorimeter Photon 1 provides photon detection and energy measurements.

M2 is the fast-particle spectrometer (momentum higher than 15 GeV/c). The 1.541 T M2 magnet provides a p_t kick of 0.845 GeV/c. The magnet's end gap is covered by another LASD station. Following 14 M2 PWC planes (see Fig.1), this spectrometer also features a transition radiation detector for electron identification (ETRD) and a 10 m long RICH [6], followed by 10 m of decay region with two sets of vector drift chambers (VDC A and B) and another lead glass calorimeter Photon 2. Two trigger hodoscopes H1 and H2 are located in the M2 spectrometer as well.

The third magnet operates at 1.3 T, equivalent to a p_t kick of 0.72 GeV/c, and is installed 42 m downstream of the charm target. The third spectrometer M3 enhances the acceptance for decays of long-lived hyperon states. Again there are PWCs, DCs, a lead glass calorimeter Photon 3, and finally a hadronic calorimeter (NCAL).

The main objective of the experiment is production and spectroscopy of charmed baryons, i.e. short–lived particles of neutral or positive charge produced by a beam–target interaction. The trigger looks for a secondary vertex and at least two fast positive particles. A typical reaction is $\Lambda_c^+ \to pK^-\pi^+$.

Two hodoscopes deployed downstream of the second magnet determine the charged particle multiplicity there. Since online vertex reconstruction would

be too slow for triggering, *SELEX* follows the idea of an impact parameter trigger: if a valid beam track and a vertex are found, the event is only accepted if they don't match. The miss distance or impact parameter is required to be larger than 20 μm. The *SELEX* trigger was designed as a four–level trigger, where the last one is a software trigger. A schematic layout of the trigger is shown in Fig. 2.

The first trigger level $T0$ fires if a valid beam definition coincides with ready state of the apparatus. The decision when to clear the silicon detectors was also done at the $T0$ level. The $T0$ signal provided the synchronization for the complete experiment.

The second trigger level $T1$ decision is formed from BTRD and multiplicity information. Coincidence of $T0$ with $T1$ passes the event to the third trigger level $T2$, which was established to include information from slower or downstream detectors in the readout.

If the event passes these three levels, all subsystems are read out into dual-ported memories. The event is analyzed by online filtering software running on a multi-processor SGI Challenge.

This filter process includes a partial reconstruction of the primary vertex, using the beam track and fast outgoing track reconstructed in silicon detector and PWCs after M2. If one or more high momentum tracks missing the primary vertex by at least 2.5 σ, event is written to hard disk and later to tape. Buffering the data on disk is necessary because tape drives would not be able to keep up with the peak data flow rate during the spill. Furthermore, disk buffering serves as a safety measure in the case of failing tape drives.

Along with charm physics, non-charm, or *beam* physics topics are major interests in E781. There are three beam physics triggers implemented in conjunction with charm physics. The following beam triggers are generated:

- *He* trigger, which looks for final states with 2 negatively charged particles.
- The hyperon, or *Hyp*, trigger, which demands a single charged particle in the target region and 3 charged particles downstream
- The exclusive, or *Ex* trigger, looks for final states with 3-5 charged particles. The photon detection system play am important role in the low-multiplicity physics with these triggers. This will be discussed in detail later.

3 The design of the lead glass calorimeter

One of the main requirements for successful experiments in modern hadron spectroscopy is a possibility to detect not only charged secondaries, but neutral ones as well, i.e. photons from radiative decays of secondary hadrons: $\pi^0 \rightarrow \gamma\gamma$, $\eta \rightarrow \gamma\gamma$, $\Sigma^0 \rightarrow \Lambda\gamma$, etc.

The photon detection system of the *SELEX* spectrometer is an essential part of the experiment. It is used in different parts of the experimental pro-

gram – in the study of charmed physics, electromagnetic formfactors of hyperons, i.e. processes in the Coulomb field of nuclei (measurements of pions polarizability and radiative widths of hadrons, search for exotic mesons), in the search for charmed pentaquarks and cryptoexotic strange baryons with additional hidden strangeness, etc.

3.1 General layout

As was mentioned above, the *SELEX* spectrometer consists of three independent spectrometers called M1, M2, M3, which include Photon 1, 2 and 3 calorimeters. Technically, each of these sections represents a completely independent system. The E781 photon calorimeters are designed to cover a large photon energy range extending to 20, 50 and 500 GeV for Photon 1, 2 and 3 respectively. Each calorimeter has a modular structure with 630, 726, 316 lead glass counters for Photon 1, 2 and 3 respectively . Each detector features a hole for the beam that did not interact in the target box. The structure of Photon detectors is detailed in Table 1.

The beam view of Photon 1 is shown in Fig. 3. It is placed at a distance of 5.37 m from the center of the target box covering polar angle interval between 20 and 100 mrad. The lateral dimensions of Photon 1 are 136.9 cm in the horizontal direction (X) and 111 cm in the vertical direction (Y). A rectangular area of 42.5×16.5 cm^2, symmetric with respect to the center of the array, is left open for the fast particles that are analyzed by downstream system.

The beam view of Photon 2 is shown in Fig. 4. It is placed at a distance of 35.67 m from the center of the target box subtending polar angles between 7 and 20 mrad. The lateral dimensions of Photon 2 are 230.9 cm in X and 110.6 cm in Y. A hole of 50.7×41.2 cm^2 is symmetric w.r.t. the center of the array.

The beam view of Photon 3, built of the elements of the E704 detector [7], is shown in Fig. 5. It is placed at a distance of 50 m from the center of the target box subtending polar angles interval between 0 and 7 mrad. The lateral dimensions of Photon 3 are 80 cm in X and 61 cm in Y. A hole of 15.2×7.6 cm^2 is shifted by 13.3 cm to the left of the array center when looking downstream.

Each calorimeter is enclosed in a metal housing. The housing protects the lead glass detectors from outside light and magnetic fields. It also serves as a hermetic volume to flush photomultiplier bases with neutral dry nitrogen gas in order to avoid phototube instabilities caused by moisture and heating.

3.2 Movable stands of Photon detector.

Two different techniques were used to calibrate the Photon Calorimeters. The first technique was to expose each block to electrons of known energies. In the second approach, the energies of photons incident on the lead glass array were determined using the kinematics of π^0 decays.

To perform the calibration and for beam tests, the entire assembly of each Photon detector is installed on a movable stand. These stands with movable platforms have been constructed by ITEP (Moscow) and IHEP (Protvino) and are mounted on rails at the *SELEX* experimental area of the Tevatron accelerator.

Electric motors (off 2.2 kW for Photon 1, 2 and 3.0 kW for Photon 3) move the stands vertically. Each stand is equipped with limit switches for the movable platform and with string position sensors connected with the FERMILAB EPICURE [8] slow control system for computer readout. The distance between the end switches is 1000 mm for the Photon 1 stand, 1300 mm for the Photon 2 stand, and 640 mm for the Photon 3 stand.

Power control circuitry is assembled in racks installed near each Photon detector. It contains temperature-controlled switches, relays for motor control, controls for motor direction of motion (a phase inverter), power connectors with the stands, connectors with the EPICURE computer interface rack, and light indicators of motion direction.

Tests were made to prepare the motion control system and position readout for calibration. Speed of motion is measured as 2.00 mm/sec for Photons 1 and 2 and 4.00 mm/sec for Photon 3. Vertical position of the movable platform is monitored with good linearity and accuracy to better than 0.5 mm using string position sensors within the motion range. Details of the beam calibration procedure are given below.

3.3 Lead-glass counters

The layout of a lead-glass counter is shown in Fig. 6. Its main components are a lead-glass block and a photomultiplier.

Three types of lead glass (see Table 2 for details) are used for Photon calorimeters. The 576 inner blocks of Photon 1 and 540 inner blocks of Photon 2, with dimensions of $42.5 \times 42.5 \times 340$ mm^3 each, are made of TF1-type lead glass. Density of the TF1 lead glass is 3.86 g/cm^3, and radiation length of the counters is 2.8 cm with 5% accuracy.

The size of the inner lead-glass block is chosen for position resolution. For a photon incident on the middle of the block one wants the shower energy to spread out to neighboring counters, so that a precise measurement of shower position using the shower profile can be made. A finer sampling of the shower

should enhance the position accuracy, while the reduced amplitude per counter leads to larger statistical fluctuations in energy. The optimal solution for shower containment is known to be a 3x3 counter, i.e., when the energy of a photon aimed at the middle of a block is fully contained in its 8 nearest neighbors plus itself.

Lead glass type F8 is used in 54 outer blocks of Photon 1 and for 186 outer blocks of Photon 2 with the sizes of $85 \times 85 \times 340$ mm^3. Density of the F8 lead glass is 3.6 g/cm^3 and radiation length of the counters is 3.1 cm.

The dimensions of all 316 lead-glass blocks of Photon 3 are $38.1 \times 38.1 \times 450$ mm^3. They are made of two types (TF1 and TF101) of lead-glass with slightly different physical and chemical properties. The counters made of most radiation resistant lead glass TF101 are used for the 128 central blocks of the detector. Density of the TF101 lead glass is 3.86 g/cm^3 and radiation length of the counters is 2.8 cm.

Degradation of the optical properties of lead glass because of radiation damages was significant in the *SELEX* experiment. The choice of TF101 material for the central part of Photon 3 was motivated by its radiation hardness. We have closely monitored glass irradiation as reported below.

Cherenkov light emitted by electromagnetic showers is detected by photomultiplier tubes (PMT). PMT FEU-84-3 with photocathode diameter of 34 mm are used in Photon 3 and in small counters of Photons 1 and 2. The Cherenkov light produced in the big blocks of Photons 1 and 2 is detected by PMT FEU-110 with photocathode diameter of 68 mm.

An ordinary magnetic shield allowed Photon 2 to work in magnetic field up to 6-8 Gauss. As seen in Fig. 1, the distance between Photon 1 and the center of the M2 magnet is about 1 m, and the field could reach up to 20-30 Gauss. The PMT is protected from the magnetic field by the shield made of a $\mu-$metal and soft steel. In Photons 1 and 2, the tubes FEU-84-3 and small lead-glass blocks are optically coupled via Silicon Rubber Compound RTV-615 (General Electric) lightguides with refractive index 1.405 made in the form of *cookies*. They are combined with plexiglass plates to provide optical contact between a big lead-glass block and FEU-110. The *cookies* sizes are presented in Table 3. For Photon 3, Silicon Rubber SILGARD is used. A plastic flange glued to the lead glass block serves as a holder for the PMT with its base and as magnetic shielding. Test results of magnetic shielding efficiency confirmed that the local magnetic shielding combined with an iron box provide satisfactory magnetic screen for Photon's PMTs. An optical fiber is attached to the front face of each lead glass counter to deliver light pulses from the monitoring system.

3.4 High voltage system

For efficient use of HV supplies tubes with similar gains are grouped in sets of 10. Each set is powered by one channel of an 1440 LeCroy 1440 power supply HV system. Each HV channel is independently programmable, which is particularly convenient during calibration runs, enabling separate adjustment of HV on groups of PMTs. Fine tuning of the HV in each PMT is done with the help of potentiometer installed on the calorimeters.

Booster power supply (BPS) modules are used to maintain PMT gain stability in Photon 3 where detector occupancy is high. These BPS modules maintain constant voltages on the last four dynodes, independent of rate. The achieved voltage stability is better than 10^{-3} with beam intensity of 1 MHz.

Four modules of BPS are housed in single crate which moves with Photon 3. The BPS crate has a voltmeter to set the selected booster voltage in each module in sequence and to monitor current consumption by PMTs during the beam run.

4 Readout electronics

The PMT output is directly connected via 66-m-long coaxial delay cables to the ADC analog inputs. In E781, LeCroy 1881M FASTBUS ADCs were used to read out the Photon calorimeters. The FASTBUS crates are housed in racks which are cooled by chilled water. The temperature of the crate is monitored by the EPICURE readout, which reads the temperature sensors installed in the rack. Inside the crate, ADC modules are controlled through FASTBUS Smart Crate Controller (FSCC)[9]. The FSCC is basically a diskless single user and multiple task computer. Each FSCC contains a Motorola 68030 microprocessor with 1 MB RAM and Ethernet interface.

4.1 ADC

The LeCroy Model 1881M provides 64 channels of analog to digital conversion in the FASTBUS format. It is designed for elementary particle and nuclear physics experiments and was developed to meet the fast conversion time needs of modern experiments.

The 1881M Analog to Digital Converter offers an approximately 12 μs conversion time for all 64 channels. It has 50 fC least count with a full 13 bits of dynamic range above pedestal for each channel. Permissible gate widths may vary from 50 to 500 ns. Each 1881M has 64 channels of front panel input and a single gate input. Events are stored in an on-board sixty four event cyclic buffer

memory. A threshold memory permits the loading of a separate constant for each channel, which is used to suppress unwanted data. Both front panel control inputs are differential ECL and are terminated by a balanced 102 Ohm impedance matching network. The terminations may be disconnected using jumpers to allow daisy chaining of modules.

Once the control and status registers have been properly programmed, the module is in acquisition mode and ready to accept a gate pulse. The duration of the gate pulse defines the acquisition phase. The gate may be provided either via a front panel ECL input or FASTBUS TR1 and TR2. For the duration of this gate signal, each of the 64 individual inputs integrate the charge applied to them. Immediately following this acquisition phase, the data is converted to a digital representation and then placed in a multi-event buffer to await readout. If sparsification is selected, data is discarded from channels that are below their individual thresholds. The data is thus 'sparsified' (also known as zero suppression), so that signals on the front end inputs less than the programmed threshold values are not buffered. Using this method, it is not necessary to transmit unwanted data over FASTBUS.

A fast clear may be applied to the module any time from 100ns after the end of the gate until the end of the Fast Clear Window (FCW). If a fast clear is applied during this period, the event currently being converted will be discarded. There is no restriction within the 1881M of the maximum FCW that may be applied externally. Clears should not be applied outside of the fast clear window.

The data of the 1881M is stored as a 32 bit word, each of which contains charge data, channel number, the geographic address and a word parity bit.

4.2 Local Trigger Logic for ADC

The function of the local trigger logic for ADCs is to take the trigger signals from global trigger logic and fan them out in the proper shape with proper timing to the ADC modules. It should satisfy following requirements:

- The gates must be timed to include all the signal but not be too wide and hence include noise.
- A clear signal must be generated once the event is rejected. The next gate can only come in no less than 800 ns and this time is controlled by the global trigger logic.
- As long as the signal is being processed, a BUSY signal must be generated to prevent further global trigger signals from occurring. And this status will be maintained until the LeCroy 1881M puts the data into its buffer and is ready to the next event. The length of this time period is fixed at 15 μs at ADC local trigger logic.
- The BUSY signal is also generated when the ADC has too many unread

events in its buffer. In the design, the latter number is limited to 32, half of the number of events that ADC can handle.

A simple logic was designed to attain the above goals. As shown in Fig. 7, the trigger units consist of a gate generator (LeCroy 222), discriminators (LeCroy 623B), linear and logical fan-out modules (LeCroy 428F and 429A), and NIM-ECL convertors (LeCroy 4616).

The pulse $T1$ arrives to the input of discriminator, and is distributed to the LeCroy 428F and 429A modules. The outputs from these fan-out modules are then sent to LeCroy 4616 to be converted into ECL signals, required by the ADC modules.

After $T1$ comes and gates to ADC are generated, conversion of the signals is started in LeCroy 1881M. The gate is generated some 30 ns after arrival of $T1$ at the discriminator. To obtain correct timing, the trigger pulse is delayed before reaching the ADC modules. (This is indicated by the vertical dashed line in Fig. 7.) Because this delay should be the same for those ADCs which read out data from the same Photon, the delaye time was adjusted detector by detector.

The fan-out modules have multiple ORed inputs. Therefore, in addition to $T1$ input, the other sources were also connected. These include the gates for probing the pedestal, for LED testing and for laser testing. These inputs also were properly delayed before they reach this point.

The next trigger signal is either $T2$ or $\bar{T}2$, depending on whether the event is accepted or rejected. In the accepted event case, the $T2$ is connected to the inputs of two LeCroy 222 gate generators. The first generator is setup for 14 μs delay. The delayed output is used as the strobe to FSCC, telling FSCC to start reading data from ADC. The NIM output of the second LeCroy 222 is taken as the BUSY signal, sent back to the global trigger system to inhibit the next trigger while conversion is in process. This BUSY signal lasts about 15 μs. It is also ORed with two outputs called THO (Trigger Hold Output) from FSCC. THO is setup in such a way that once there are more than 32 events accumulated in the ADC buffer, it becomes TRUE. Therefore, when there are 32 unread events in the ADC buffer, the BUSY will take effect until the next event is read out from ADC. The 1 μs difference between these two gate generators eliminates the gap between the ADC conversion BUSY and the FSCC readout BUSY.

In rejected event situation, $\bar{T}2$ will generate clear signals for all ADCs to clear the data. After clearing, the ADC is ready to accept the next event.

The timings for these two situations are illustrated in Fig. 8. In this picture $T12$ is determined by global trigger logic, defining time difference between $T1$ and $T2$. Td is delay adjusted detector by detector to obtain correct timing.

4.3 Photon 3 trigger

As was mentioned above, the total energy deposit in Photon 3 was included in the exclusive trigger. The scheme of the trigger is presented in Fig. 9. For the tubes in each column a sensitive divider sends 5% of the current to a linear shaper. The column sums are added in a second unit. Finally, a discriminator generates the $T2$ trigger signal if the energy exceeds threshold.

5 Overview of the monitoring system

Changes in the temperature of the PMT and the electronics, as well as glass transparency degradation because of radiation damage, could cause long and short term variations of the amplitudes of signals read out from the lead glass counters. Therefore, calibration constants of each lead-glass counter must be monitored throughout the long periods between electron beam calibration. The monitoring system is responsible for the following tasks:

- Monitoring of the readout of all channels by sending short light pulses *during* and *between* beam bursts.
- Linearization of each readout channel. The linearity of the response is checked over the full dynamic range. For channels with non-linear response, appropriate corrections are introduced.

The scheme of the monitoring system is shown in Fig. 10. It includes two independent systems based on Light Emitting Diodes (LED) and on a high-powered ultraviolet (UV) laser.

5.1 LED monitoring system

The LED monitoring system delivers short pulses via optical fibers to each counter. The main elements of this monitoring system are:

- the light distribution system,
- the system of LED light pulse sources (red, orange),
- the system of PIN photodiodes with high stability.

The light distribution system supplies light pulses with fixed amplitudes into each of 1680 readout channels. As mentioned above, the front panel covering the lead glass array has a 1 mm hole for inserting a single optical fiber, that is fixed by a rubber washer and a nut. The front plane is protected from outside light by a removable cover. The light distribution system is installed in the

space between the front plane and the cover.

Each calorimeter has a light distribution box (LB) which mixes an input light pulse from an optical source into quasi-uniform light pulses on the optical fiber network that goes to each lead glass block. The light box consists of a cylindrical plastic box, with length of ≈ 10 cm and diameter of ≈ 4 cm, and of a light source.

The light source is based on red LEDs [5] for Photons 1 and 2 and on red and orange LEDs for Photon 3. Each LED is fired by a short (100 ns) signal provided by a pulser.

The fiber bundles for Photons 1 and 2 consist of glass fibers with diameter of ≈ 2 mm and length of ≈ 200 cm. The fiber bundle for Photon 3 consists of plastic fibers that are glued together forming a rigid structure with a diameter of ≈ 3 cm. The fiber ends are cut and polished to provide good light transmission. Each fiber has a diameter of ≈ 1 mm and a variable length of $\approx 20 - 80$ cm, adjusted so as to reach all Photon 3 channels.

Because LED output intencity varies a lot, pulse height normalization is done using photodiodes. Two photodiode/preamp (PD) circuits housed in RF-shielded boxes are optically coupled to the light distribution box via fibers. The photodiode assembly consists of two identical channels. Two PIN photodiodes couple to a fast preamplifier, specially designed for *SELEX* by the Tel-Aviv University group. The photodiode Hamamatsu S1223-03 has been chosen, as it has sufficiently large bandwidth of 20 MHz, large active area of 3.6×3.6 mm^2, large spectral range of $320 - 1100$ nm, and low temperature coefficient of $\approx 0.1\%/^oC$ [6]. The incident light pulse is injected via optical fibers and focused by small lenses on the active surface of the diodes. Their responses to incident light are linear over the range of equivalent light-energy of each calorimeter, and stable over long periods of continuous operation. The monitoring system provides normalization of the photodiode signals with $<1\%$ stability.

5.2 Laser monitoring system

As mentioned above, the Photon calorimeters are positioned at large distances from the target box and have very different dynamic ranges. They operated in the energy range 1-500 GeV. To overcome transmission losses and still deliver a large dynamics range of energy-equivalent light intensity requires a laser light source. The laser system based in a Laser Photonics LN300C is used for monitoring of all three Photon spectrometers simultaneously, to perform phototube readout linearity and timing tests, and to simulate the *SELEX*

[5] red LED, type AND190GRP, 10 mm package, I(MCD@20mA)=13000, view angle 4^o, manufactured by Hewlett Packard

[6] Hamamatsu photodiodes, Cat. KPD0001E02, Feb. 94

trigger for Photon calorimeters in the absence of the beam. Its main elements are:

- a high-power UV N_2 laser coupled to a dye laser module,
- a remotely controlled wheel containing several neutral density filters to attenuate the laser beam,
- the first light distribution stage located near the laser, which splits the beam into fibers running out to all Photon calorimeters.

The primary laser light distribution system (see Fig. 10(b)) consists of a laser and a simple optical system to control the amplitude/timing of light pulse and then to deliver it to the light distribution system via a long optical fiber.

The N_2 laser with an energy of 280 μJ/pulse emits short 4 ns pulses with the wavelength of 337 nm at a rate of 1-30 Hz. It is used for pumping a dye laser. A blue dye with peak emission at 425 nm and a conversion efficiency of 20% is used. The "colored" light beam enters an aluminium box, which contains the first PIN photodiode used for timing (PD-T), a computer controlled electromagnetic shutter, a set of 12 calibrated neutral density filters mounted on a computer controlled wheel, a second PIN photodiode measuring the pulse amplitude (PD-A) and, finally, the injector of the light pulse into an optical fiber with the diameter of 1 mm and length of $\sim$ 80 m.

The light splitter distributes the laser light pulse to the calorimeters in proportion to their dynamic ranges and number of lead-glass blocks.

As Photon 1-3 calorimeters have dynamic ranges of 20, 50, 500 GeV and consist of 630, 726 and 316 lead-glass counters, respectively, the light pulse amplitude is split in a proportion of 7/20/100.

5.3 Monitoring procedure

The accelerator supplies beam particles for 20 s out of each 60 s. The time between bursts is used for monitoring. At interspill time gates are provided via CAMAC by Fermilab 040 Pulse train units with 3 independent outputs each, located in CAMAC crate (Fig. 11). Output 1 provides gate signal for ADC pedestal measurement with the same electronics as in $T1$, Output 2 is split into two signals: the first is used to trigger the LED signal and the second to generate the gate measuring the detector response.

Every detector has its own LED system, which produces light pulses and distributes them over the detector. The second signal, after a certain delay, is delivered to the LeCroy 623 discriminator, and then to the $T1$ gate system. Output 3 is used for laser measurement. It sends the trigger signal to the laser and at the same time produces the gate to measure the pedestals. The laser trigger signal is sent over about 100 m cable to the laser, where it is converted to a TTL 5-μs-wide signal. On this trigger, the laser fires and the light pulse is

transported back to the experimental hall via an optical fiber, and delivered to Photons 1,2, and 3. The laser light pulse is also detected by two photodiodes (PD-T and PD-A) as described in previous section. PD-T fast timing signal is sent to the experimental hall synchronously with the light pulse and detected by discriminator to be fed to the rest of the $T1$ system and to produce the ADC gate.

The ADC calibration monitoring program, **mon**, is used to record basic parameters of the detectors. The program runs independently on the FSCC computer in the ADC FASTBUS crate under the control of master crate resident program. Master spawns **mon**, awakes it during interspill time and makes it sleep during the spill. For every ADC channel connected to the detector, **mon** computes the following values:

- the average ADC response,
- rms of external light signal, either LED or laser,
- ADC response without any light signal (pedestal).

The program estimates the quality of these values and compares them with those obtained earlier, which are considered as a stable reference. These earlier data are stored in a work data base. **Mon** also produces an output file, histoscope files to be used to evaluate detectors, and files containing ADC thresholds. These thresholds are set slightly above the pedestal's mean values, to be used to suppress noisy channels in the ADC sparse mode used for data-taking.

6 Test of the Lead Glass Calorimeters

As mentioned above, in the *SELEX* experiment the PMTs experienced significant stray magnetic fields. The magnet nearest to Photon 1, M2, generates a magnetic field $H \leq 13$ kG (absolute value) in the magnetic gap. The LED monitoring system is used for study field effect. The amplitudes of LED signals were obtained for the following four cases:

1. $A_{initial}$ for magnetic field H = 0, before switching the magnet in;
2. A_+ for H = +13 kGs, positive current I = +2500 A;
3. A_- for H = −13 kGs, negative current I = −2500 A;
4. A_{final} for H = 0, after switched the magnet off.

We measured the following amplitude changes:

$\Delta_{+i} = (A_+ - A_{initial})/A_{initial} = (-22 \pm 4) * 10^{-4}$
$\Delta_{-i} = (A_- - A_{initial})/A_{initial} = (-0.4 \pm 3.5) * 10^{-4}$
$\Delta_{+-} = (A_+ - A_-)/A_- = (-19 \pm 4) * 10^{-4}$

$\Delta_{+f} = (A_+ - A_{final})/A_{final} = (24 \pm 3) * 10^{-4}$
$\Delta_{-f} = (A_- - A_{final})/A_{final} = (3 \pm 4) * 10^{-4}$
$\Delta_{fi} = (A_{final} - A_{initial})/A_{initial} = (5 \pm 2) * 10^{-4}$

All differences in amplitudes are well below 1%. These results confirm that the local magnetic shielding combined with iron box of the detector provide satisfactory magnetic screen for the Photon PMTs.

6.1 Space resolution studies

Space resolution was estimated using electrons from the calibration data set. Detector space resolution is influenced by transverse dimensions of the electromagnetic shower as well as by the size of the lead glass counter. To measure the shower profile, a ratio of the amplitudes in two neighboring blocks was measured as a function of the coordinate of the entry point of the electron beam. Transverse size of the shower is determined by the Moliere radius R_M,

$$R_M = X_0 E_S / E_C, \tag{1}$$

where the scale energy $E_S \approx 21$ MeV, E_C for the TF1 lead-glass block is 15 MeV, and X_0 is 2.5 cm. Observed sizes of showers are consistent with a Moliere radius value of $R_M = 3.5$ cm for the lead glass.

The data of calibration runs were used to estimate the value of space resolution of the detector as a function of beam position. The position resolution was found to vary in the range of $2.0 - 5.5$ mm, improving from the center towards the edge of the central block.

6.2 The depth correction studies

If the photon angle of incidence is not 90^0, the transverse position of the photon impact point into the calorimeter and of the shower maximum are not the same. The corresponding correction can be derived experimentally by studying the showers from electrons hitting the lead glass at different angles.

Electrons were taken from charm trigger runs and from runs with a special trigger (Section 2). *SELEX* track reconstruction determines the trajectory, its entry point r_{act} and angle θ in the lead glass block. The center of gravity of the electron shower (r_{clus}) is calculated. The depth correction ($r_{clus} - r_{act}$) defines the shower depth:

$$D = (r_{clus} - r_{act})/\sin\ \theta. \tag{2}$$

It was found that the best average value of the shower depth D over all energies for Photon calorimeters is about 16 $\pm$ 3.5 cm. For Photon 3 this correction is unnecessary, it accepts only photons with angles $<$ 8 mrad.

7 Calibration of the Lead Glass Calorimeters

7.1 Event reconstruction

The algorithms for the reconstructing particles in lead glass calorimeters are described in [10],[11]. Photon reconstruction program is integrated into the *SELEX* Off-line Analysis Program (SOAP). The Photon data base contains the information about geometry, ADC-block mapping, PMT gains, pedestals and other information needed for reconstruction. Reconstruction starts with finding the hit counters and their energy depositions. If the energy deposited in the counter exceeds a certain limit, the corresponding channel is used further to form first stage clusters. At the next step, the program starts searching for coordinates of local maxima in each cluster. After that impact point of the particle that hit the calorimeter are reconstructed.

When several photons hit the calorimeter close to each other, the problem of reconstruction becomes more complicated due to overlapping of clusters. One of the reconstruction methods is to separate such clusters and fit two-dimensional functions with the set of detected amplitudes, varying the impact coordinates and photon energies. Unfortunately, this algorithm is very CPU time consuming. Here an alternative method is used.

After finding the maxima in the first stage clustering, the comparison of each shower shape with the "ideal" one is made in terms of χ^2. The database contains shower libraries for three types of lead-glass blocks according to the type of the glass and the block sizes. The aim of this database is to describe the shape of the shower in terms of the cluster *center of gravity* coordinates. If there is a cluster with a center of gravity coordinate (X_C, Y_C) and a cell (counter) with the coordinates (X,Y), then the function $phot\_cell(X - X_C, Y - Y_C)$ returns the energy in the cell for the case when the shower is electromagnetic and ideal (no fluctuations). Then program compares this value with the measured one and calculates χ^2. If this χ^2 is satisfactory ($\chi^2 \leq \chi^2_{max}$), the cluster is accepted as a γ, otherwise separation using an iterative procedure is performed, introducing a second photon peak, based on positions of local peaks. Cluster matches neutral hadrons if χ^2 remains high after all iterations. For particle identification, track information from the *SELEX* spectrometer is used to estimate the impact point of all charged tracks. For each cluster, the difference x_r between the nearest impact point and the cluster center is calculated. If x_r exceeds the limit h_r (maximum hadronic linkage radius) the cluster is considered as a "photon". Usually $h_r = 5$ cm, but the value of h_r may depend on physics goals. A cluster with $x_r \leq h_r$ is classified as electron, muon or charged hadron depending on χ^2 values of energy, reconstructed momentum and cluster dimensions.

7.2 Calibration of detectors

The calorimeters were calibrated by dedicated electron beam runs several times during the data taking. Generally, each calibration represents a series of exposures to electrons of known energies to obtain calibration constants for all channels of the Photon calorimeters. During calibration, moving platforms shifted the calorimeter in the vertical direction in order to place each counter in the beam. Horizontal deflection was provided by the experiment magnets. However the calorimeter response to photons and electrons is slightly different[12]. To obtain more accurate calibration constants, π^0 data from real events is used. The next step includes selecting two-gamma events and performing calibration using two-photon constrained fitting.

7.3 Event selection for π^0 calibration

To perform a π^0 calibration, "Exclusive" trigger data have been analyzed. Two-gamma events with each gamma having energy of 5 GeV and more and with total energy above 15 GeV are selected. The dimension of the clusters produced by Photons has been chosen to be more than 2 counters in order to reduce the background. Any photon candidate that has an Y-coordinate the same as for any other reconstructed particle in the same Photon detector within 4 mm is dropped; it has too large a probability of being affected by bremsstrahlung, scattering or gamma conversion. If fewer than two gammas in Photon 2 and 3 survived after applying the cuts mentioned above, an additional search for photons was performed in Photon 1 with a lower photon energy threshold of 0.5 GeV. To reduce the size of output data, events with the 2γ invariant mass less then 50 MeV were dropped. Events with total multiplicity greater than 15 were rejected to reduce combinatorial background.

Initial calibration constants are computed from the electron calibration corrected by LED monitoring:

$$G = G_0 \times \frac{A^{LED}}{A_0^{LED}}, \tag{3}$$

where G and G_0 are the gains for the current and calibration runs, respectively, and A^{LED} and A_0^{LED} are the amplitudes of corresponding LED signals.

Next, from the set of events selected for π^0 calibration, events in which a single counter had more than half the cluster energy were selected. The $\gamma - \gamma$ mass distribution was fitted by polynomial with a Gaussian function. The gain of counter i was corrected iteratively :

$$G(k+1)_i = G(k)_i * \sqrt{M(\pi^0)_{PDG}/M(\pi^0)_{fit}}. \tag{4}$$

where k is the number of iterations performed, $M(\pi^0)_{PDG}$ is π^0 mass from PDG [13] and $M(\pi^0)_{fit}$ is π^0 mass calulated for π^0 candidates in given event. New gain factors G_i were calculated after each iteration as a mean value of all iterations $(G_i(1), ..., G_i(k+1))$. The iteration sequence converges in about 20 iterations. Photons 2 and 3 were calibrated first, then calibration for Photon 1 was done. And finally, the same procedure was performed on standard runs with the Charm trigger. New tables with gains are created for each group of about 100 runs.

7.4 π^0 calibration results

The parameters of 2γ invariant mass spectrum are obtained for new set of calibration coefficients obtained using two-photon constrained fitting. The only cut used here was the cut on gamma energy, and mass spectrum was fitted with a simple Gaussian distribution. We consider events where both gammas hit Photon 1 - "11", both gammas hit Photon 2 -"22" and both gammas hit Photon 3 "33". We also look at the events where one gamma hit Photon 1 and second hit Photon 2 -"12", first gamma hit Photon 1 and second hit Photon 3 -"13" . and where first gamma hit Photon 2 and second hit Photon 3 -"23" . Here we consider only isolated gammas with $E_\gamma > 2$ GeV and not near the border/hole of detectors. The results of fitting of the π^0 mass for events obtained with the Charm trigger are presented in Fig.12 and Table 4. The typical systematic π^0 mass shift is less than 0.5 MeV/c^2 except Photon 1 where the shift is 1.2 MeV/c^2. As expected the best resolution is obtained with Photon 2 detector, where the space and energy resolutions for photons are optimal.

8 Photon detectors monitoring during data taking

The long-term stability of each calorimeter was checked by monitoring the values of the ADC pedestals and the gain values. It was found that they were stable within a few percent during the entire time of operation. Fig. 13 shows the values of pedestals observed over several months running period for three typical modules. When the values of pedestals changed significantly, the data base was updated. The largest variations are usually related to runs recorded just after long shutdowns. The reason is that some time is needed to reach the normal temperature conditions of electronics.

8.1 Monitoring of the radiation damage

Several studies of the radiative damage for different types of lead glass Cherenkov counters in γ spectrometers were performed with different beams of high energy particles. Lead glass radiation damage in *SELEX* Photon detectors is monitored with two light sources: the light emitting diode LED which provides red light, and the dye laser (LSR) tuned to green light. It was found that in our range of exposed dose, red light from the LED passes through the glass without considerable attenuation, and even after one year of glass irradiation the attenuation does not change significantly. So relative variation of the PMT signal indicates instabilities of the PMT or of other electronics.

Green laser light passing through the glass has very little attenuation if the lead glass block is not damaged. After substantial irradiation (a few hundred *rad* for standard lead glass and about 10000 *rad* for radiation hard glass) block transparency drops for the green light. Comparison of the signals from the LED and LSR sources allows one to determine the PMT instability and glass radiation damage.

Two monitoring measurements, the first one during the first Photon calibration runs (December 96) and the second one when the data taking was finished (September 97), were performed. Distributions of uncorrected ratios of laser signals with photodiode normalization,

$$R_{uncorr} = \frac{A'_{laser}}{A_{laser}} \tag{5}$$

where A_{laser} and A'_{laser} are the values of the PMT laser signals at the beginning (December 1996) and the end (September 1997) normalized by the amplitudes of the corresponding laser photodiode (PD-A) signals. These distributions presented as dashed histograms in the Fig. 14 show broad variations of counter signals. To estimate the effect of radiation damage, an additional correction

using corresponding LED signals is made:

$$R_{corr} = R_{uncorr} \times K_{corr}. \tag{6}$$

where

$$K_{corr} = \frac{A_{LED}}{A'_{LED}}. \tag{7}$$

Here A_{LED} and A'_{LED} are the values of the PMT LED signals at the beginning (December 1996) and the end (September 1997) of the measurements respectively, normalized by the corresponding amplitudes of the photodiode (PD-A) signals. It is expected that the blocks damaged by radiation have values of R_{corr} that are below unity due to transparency losses because of radiation damage. Distributions of R_{corr} also presented in the Fig. 14(solid histograms). Distributions on the correction coefficients K_{corr} are shown in the Fig. 15 (a), (b) and (c) for the Photon 1,2,3 respectively. Other instabilities should have a symmetric distribution, as was seen for Photon 2 big block counters. At the same time, for partially irradiated small counters the distributions are distorted since damaged counters have low values of R_{corr}. Positions of these counters in Photons 2 are presented in Fig. 16. The correlation between R_{corr} and radiation flux from the beam is clearly seen. Positions of partially irradiated counters in Photons 3 are presented in Fig. 17. The borders between radiational hard and ordinary glass is clearly seen.

Lead glass TF101 irradiated by a dose of $2 \cdot 10^4$ rad loses about 1% of the passing light on 1 radiational length[14]. For TF1 lead glass, a similar light loss is caused by an absorbed dose of $2.5 \cdot 10^2$ rad [15].

In Photon 2, only two counters have lost the transparency by factor of two or more. Applying the approximation from [15] to our glass sizes, the absorbed dose in these counters is estimated to be about 500 rad. For the counters with transparency loss of 10% or less (R_{corr}=0.8 $\div$ 0.9) the absorbed dose is about 120 rad. Several dozen counters have smaller but measurable damage.

In Photon 3, there are no visible damages of inner radiation-hard glass blocks except three blocks located near the beam hole. Estimated absorbed dose in these counters is $4 \cdot 10^3$ rad. Radiation damage of TF1-000 glass blocks placed along the border with inner radiation-hard blocks is evident, but it is partially masked by other instabilities.

There are several counters with small R_{corr} in Photon 1, but the distribution is too broad to see details of their radiation damage.

8.2 Lead Glass Transparency Monitoring During Measurements

Variations of R_{corr} during the measurements have been studied for several channels of each of Photon detectors to understand the dependence of lead glass transparency on beam intensity. The results are presented in Fig. 18 for several groups of runs where the data were available. R_{corr} is shown for a typical counter of Photon 1 (undamaged) and for two damaged counters of Photon 2 and Photon 3. Photon 1 counter has practically no monotonic variations in time apart from fluctuations to be considered below. For the counters damaged by radiation, a linear decrease of the signal with run number is observed. There are several special points in Fig. 18. There is a jump in the region of the runs 9837-9844 where a power outage took place. At that moment beam intensity decreased by a factor of 10. Correspondingly, R_{corr} is changing slowly after this point.

9 Performance of Photon detectors

9.1 Experimental data

The main aim of the *SELEX* experiment is to make a systematic survey of charm baryon production and decay mechanisms. Such a data set is needed to understand if perturbative QCD can account for charm production under different circumstances and to establish which mechanisms dominate decay processes. By having complete particle identification for hadrons, electrons, and gammas, one can normalize branching ratios to the semileptonic rates. This aids the theoretical analysis of the hadronic modes. The ability to measure π^0 and η^0 states is also important in analyzing these ratios for evidence of resonant substructure.This substructure is clearly a dominant feature of meson decay.

Also, as has been mentioned earlier, three of the expected ground state charm baryon multiplet properties have been measured with low precision: Σ_c^+, Ξ_c^+ and Ω_c^0. *SELEX* acquired a large data set containing various decay data modes of all singly charmed baryons. In excited charm baryons the Q-value of the decay is small. Therefore the deexcitation particle is slow, emitted near the baryon line of flight. For γ decays, this means that one must find a low energy photon near 0^o and separate it from the bulk of primary interaction π^0 decays.

Due to the 50 m length of the *SELEX* setup (which results in good small angle resolution), long run period, excellent tracking and the high beam energy, Primakoff physics measurements with very small momentum transfer are also feasible. Among these physics interests, we mention radiative widths of hadron resonant states, hadron radius and pion polarizability.

All goals mentioned above require a high efficiency of γ and π^0 reconstruction. To demonstrate detector sensitivity and resolution, signals from several well known particles decaying into photons are studied. The simplest test of the calibration of the Photon detectors over a wide energy range is provided by combined mass plots for events from real data. The Exclusive trigger had lower multiplicities (3 charged track in vertex and about 2.4 gammas with energy above 2 GeV on average) and allowed us to obtain clear signals of many hadronic states.

π^0 and η production was identified via their decay mode involving two photons in the final state. For this purposes we selected events in exclusive trigger in π^- beam with two γ clusters, each having energy in excess of 2 GeV and energy of 2γ system $E_{\gamma\gamma} > 10$ GeV. Fig. 19 shows the invariant mass distribution of two photons with sharp π^0 and η peaks.

The η and ω meson were separated in their decay to $\pi^+\pi^-\pi^0$. For this purposes we selected events with exclusive trigger in Σ^- beam with two γ clusters, each having energy in excess of 2 GeV and satisfied π^0 identification criteria

(mass window ± 25 MeV of PDG value[13]) together with requirement that π^- is not a leading particle. Fig. 20 shows the invariant mass distribution of $\pi^+\pi^-\pi^0$ for events with $E_{\pi 0} > 10$ GeV.

The η' and f meson were selected in the decay $\pi^+\pi^-\eta$. For this purposes we selected events with exclusive trigger in the π^- and Σ^- beam with two γ clusters, each having energy in excess of 2 GeV and satisfied η identification criteria (mass window ± 50 MeV of PDG value) together with requirement that π^- is not a leading particle. Fig. 21 shows the effective mass distribution of $\pi^+\pi^-\eta$ for events with $E_\eta > 10$ GeV.

To separate a signal from the decay $K^0 \to 2\pi^0$ we selected events with exclusive trigger in the Σ^- beam with γ clusters having energy in excess of 4 GeV and number of pairs which satisfied π^0 identification criteria (mass window ± 20 MeV of PDG value) did not exceed 4. Fig. 22 shows the effective mass distribution of $2\pi^0$ for events with $E_{\pi^0} > 30$ GeV.

The η meson was also separated in the decay $\eta \to 3\pi^0$. In this case we required that Photons recorded six γ clusters having energy in excess of 5 GeV and these clusters form three π^0 candidates (mass window ± 20 MeV of PDG value). Fig. 23 shows the effective mass distribution of $3\pi^0$ for events with $E_{\pi^0} > 20$ GeV.

Fig. 24 shows the effective mass distribution for $\pi^+\pi^-\gamma$ system. For this plot we selected events with the Exclusive trigger in the Σ^- beam with following cuts: π^- is not a leading particle, $E_\gamma > 2$ GeV, there is at least 1 γ with $E_\gamma > 50$ GeV and it didn't make a π^0 with any other γ-s, and there is only one γ with $E_\gamma > 4$ GeV in event. Four peaks clearly observed (see figure caption for their description).

In the Charm trigger where multiplicities in event is much higher (10.5 charged track in vertex region and 6 gammas on average with energy above 2 GeV) the γ identification is little bit harder but still possible. In the Charm trigger we selected events with γ clusters having energy in excess of 2 GeV. Fig. 25 shows the invariant mass distribution for energy of the 2γ system with the number of γs $N_\gamma < 10$ and $E_{\gamma\gamma} > 10$ GeV. An π^0 signal is clearly seen in this distribution, confirming our ability to do a charm physics with neutral components in final states. Of course, the cut on gamma multiplicity strongly suppress background. For the same data Fig. 26 shows the invariant mass distribution for 2γ system with energy $E_{\gamma\gamma} > 10$ GeV and the number of cluster $N_\gamma < 3$.

In the Charm trigger sample we can reconstruct hyperons even without a cut on number of clusters. Fig. 27 shows the effective mass distribution for the $\Lambda\gamma$ system with cut on γ energy $E_\gamma > 6$ GeV. No cut on number of γ-s is applied. Photon 1 is not included. The Λ is reconstructed in process $\Lambda \to p\pi^-$ and constrained to PDG [13] mass value 1115.68 MeV within 1116 ± 3 MeV mass window.

D^{*0} mesons decaying into identified $D^0 + \pi^0$ and $D^0 + \gamma$ are studied. The D^0 candidates were reconstructed in 4 modes corresponds to process $D^0 \to K^-\pi^+$, $\overline{D^0} \to K^+\pi^-$, $D^0 \to K3\pi$, $\overline{D^0} \to K3\pi$ are taken. Fig. 28 shows the mass dif-

ference distribution for $\Delta M_\gamma = M(D^0\gamma) - M(D^0)$ with the cut on γ energy $E_\gamma > 6$ GeV. $\Delta M_\gamma = 0.1412 \pm 0.0009$ Photon pairs with an invariant mass within $\pm$ 15 MeV/c^2 of the nominal π^0 mass are accepted and kinematically constrained to its value. The results are shown in the Fig. 29. $\Delta M_\gamma = 0.1420 \pm 0.0012$ The position of the observed peak is in agreement with known mass difference between D^{*0} and D^0.

10 Summary

The design and construction of three Photon calorimeters were described. These calorimeters were build to be used as part of Fermilab *SELEX* experiment E-781, a study of charmed baryons in hyperon beam. The performance and stability of calorimeters response were continuously measured during the year of data taking and the data are in good agreement with the design values and expectations. Good energy and small angle resolutions allows to perform a variety of precise measurements in both charm and non-charm physics area.

11 Acknowledgments.

The authors are grateful to the staffs of IHEP, ITEP, Fermi National Accelerator Laboratory, Carnegie Mellon University, and Tel Aviv University for technical support. Special thanks are due to L. Stutte for her contribution in setting up of ITEP-IHEP participation to the SELEX experiment and valuable discussion. This project was supported in part by the Israel Science Foundation founded by the Israel Academy of Sciences and Humanities, the International Science Foundation (ISF grant J9K100), the National Science Foundation (Phy#9602178), NATO (grant CR6.941058-1360/94), the Russian Academy of Science, Russian Foundation of Fundamental Investigations, the Russian Ministry of Science and Technology, U.S. Civilian Research & Development Foundation, the U.S. Department of Energy (DOE grant DE-FG02-91ER40664 and DOE contract number DE-AC02-76CHO3000), and the U.S.-Israel Binational Science Foundation (BSF).

References

[1] J. Wiss, *In *Varenna 1997, Heavy flavour physics* 39-93.*

[2] J. S. Russ, Nucl. Phys. A **585** (1995) 39C.

[3] M. Y. Balats *et al.*, ITEP-92-109.

[4] Yu.Goncharenko *et al.*,IHEP preprint 95-109, 1995

[5] J. Lach, FERMILAB-TM-2129, 2000.

[6] J. Engelfried *et al.*, Nucl. Instrum. Meth. A **433** (1999) 149.

[7] D. L. Adams *et al.*, IHEP preprint 91-100, 1991.

[8] E. Dambik, D. Kline and R. West, FERMILAB-CONF-93-288 *Presented at International Conference on Accelerator and Large Experimental Physics Control Systems (ICALEPCS 93), Berlin, Germany, 18-22 Oct 1993.*

[9] S. Zimmermann, V. H. Areti, G. W. Foster, U. Joshi and K. Treptow, FERMILAB-CONF-91-290 *Presented at IEEE 1991 Nuclear Science Symp., Santa Fe, NM, Nov 5-9, 1991.*

[10] A. A. Lednev, IFVE-93-153.

[11] A. A. Lednev, Nucl. Instrum. Meth. A **366**, 292 (1995).

[12] D. Autiero *et al.*, Nucl. Instrum. Meth. A **425**, 188 (1999).

[13] K. Hagiwara *et al.* [Particle Data Group Collaboration], Phys. Rev. D **66** (2002) 010001.

[14] M. Kobayashi *et al.*, Nucl. Instr. and Meth. **A 345** (1983) 210-212.

[15] A.V. Inyakin *et al.*, Nucl. Instr. and Meth. **215** (1983) 103-106.

12 Tables

Table 1: Specifications of the *SELEX* lead glass calorimeters.

	blocks		z position	transverse dimensions	
	small	large	[cm]	total [cm^2]	hole [cm^2]
Photon 1	576	54	526.6	136.9 x 111	42.5 x 16.5
Photon 2	540	186	3573.2	230.9 x 110.6	50.7 x 41.2
Photon 3	316		5003.9	80 x 61	15.2 x 7.6

Table 2: Chemical structure of lead glass.

	F8-00	TF1-000	TF101
PbO	45.0 %	51.2 %	51.2 %
SiO_2	42.8 %	41.3 %	41.5 %
K_2O	10.4 %	7.0 %	7.0 %
Na_2O	1.8 %	-	-
As_2O_3	-	0.5 %	-
CeO_2	-	-	0.2 %
Refractive index, n_e	1.62	1.65	1.65

Table 3. Cookies.

Photon	PMT	Material				Qty.
		Plexiglas		RTV615		
		O.D. (mm.)	THKNS (mm.)	O.D. (mm.)	THKNS (mm.)	
Photon 1	FEU-110	75	30	75	4	54
	FEU-84-3			30	15	576
Photon 2	FEU-110			75	4	186
	FEU-84-3			32	4	540
Photon 3	FEU-84-3			27	10	316

Table 4. π^0 calibration results.

Photon comb.	π^0 mass, MeV	π^0 width, MeV	$\sigma(M)/M$, %	γ energy range, GeV
11	133.8 ± 0.05	9.1 ± 0.1	6.5 ± 0.1	2-10 GeV
12	135.5 ± 0.1	8.4 ± 0.1	6.2 ± 0.1	
13	134.5 ± 1.2	8.6 ± 0.1	6.3 ± 0.1	
22	135.2 ± 0.1	6.4 ± 0.1	4.7 ± 0.4	2-40 GeV
23	135.2 ± 0.1	6.9 ± 0.1	5.0 ± 0.4	
33	134.6 ± 0.1	7.3 ± 0.1	5.3 ± 0.4	2-80 GeV

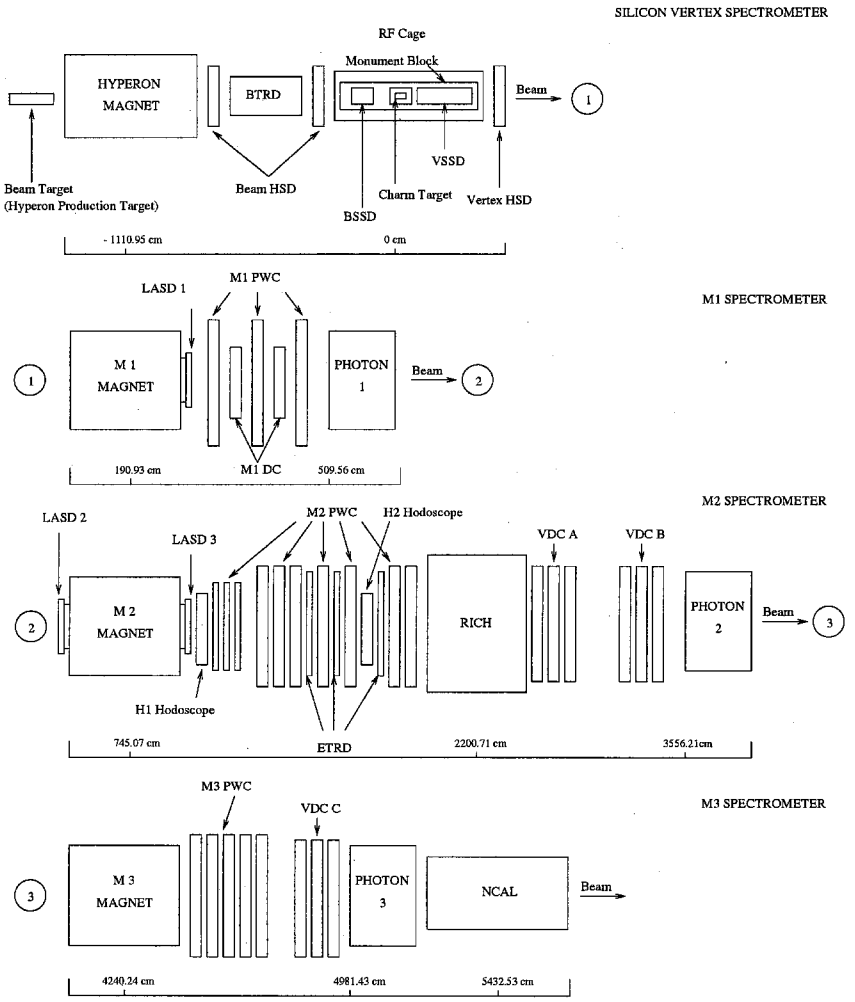

Fig. 1. Schematic diagram of the *SELEX* layout. See the text for the meaning of the labels.

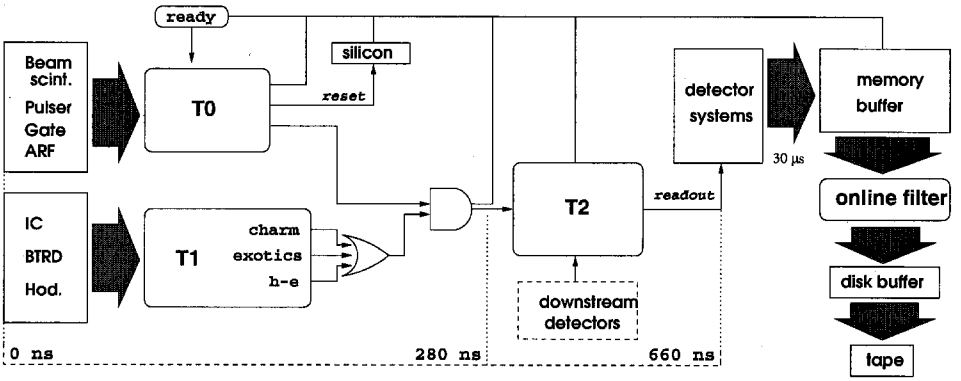

Fig. 2. A simplified scheme of the *SELEX* trigger.

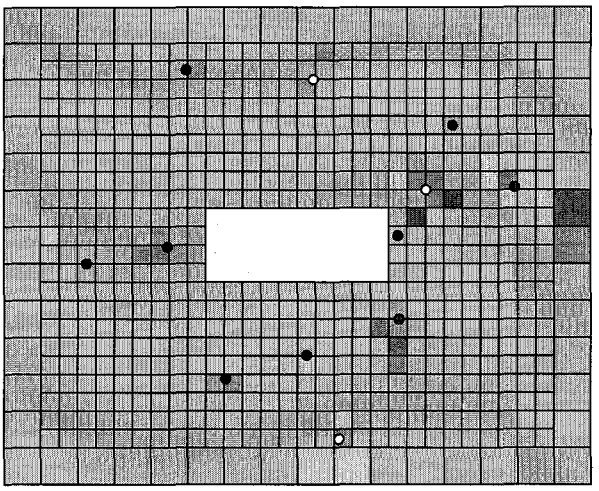

Fig. 3. Beam view of Photon 1. Colored blocks show typical energy spread in a reconstructed event. Black dots are the coordinates of the photon clusters, white dots correspond to other neutral particles, shaded dots correspond to charge particles.

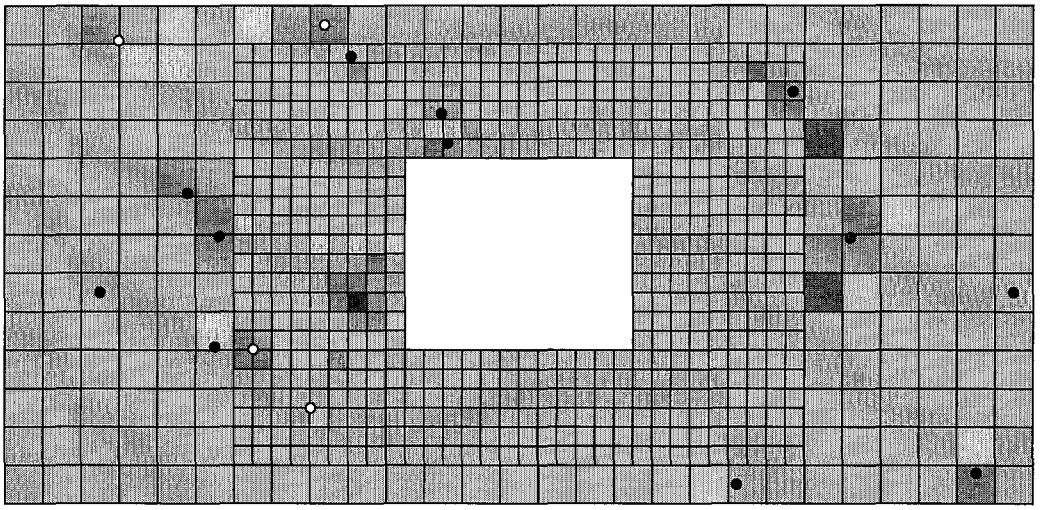

Fig. 4. Beam view of Photon 2. Colored blocks show typical energy spread in a reconstructed event. Black dots are coordinates of the photon clusters, white dots correspond to other neutral particles, shaded dots correspond to charge particles.

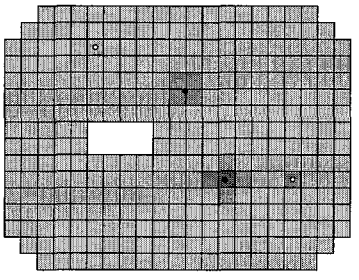

Fig. 5. Beam view of Photon 3. Colored blocks show typical energy spread in a reconstructed event. Black dots are coordinates of the photon clusters, white dots correspond to other neutral particles.

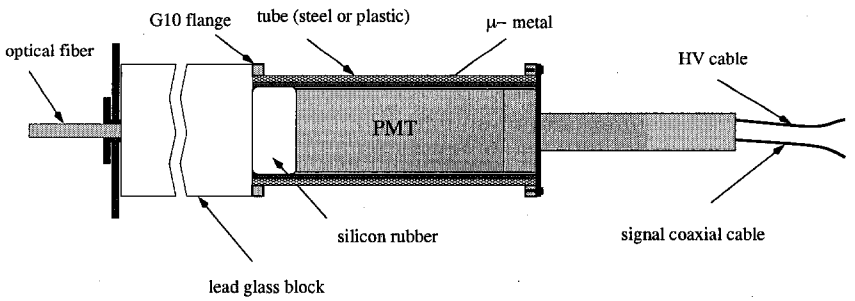

Fig. 6. Schematic layout of a lead-glass counter.

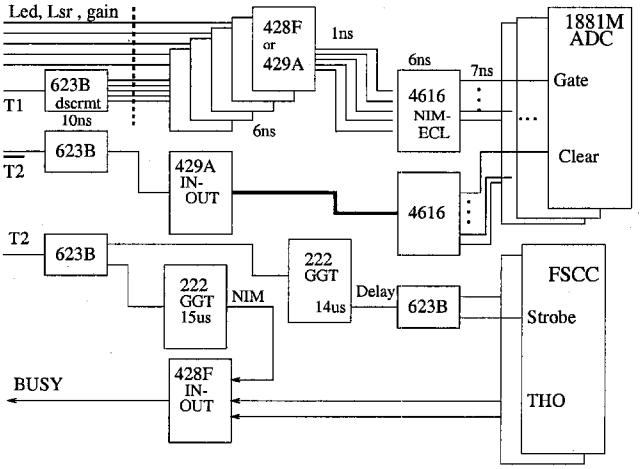

Fig. 7. Block diagram of the ADC local trigger logic.

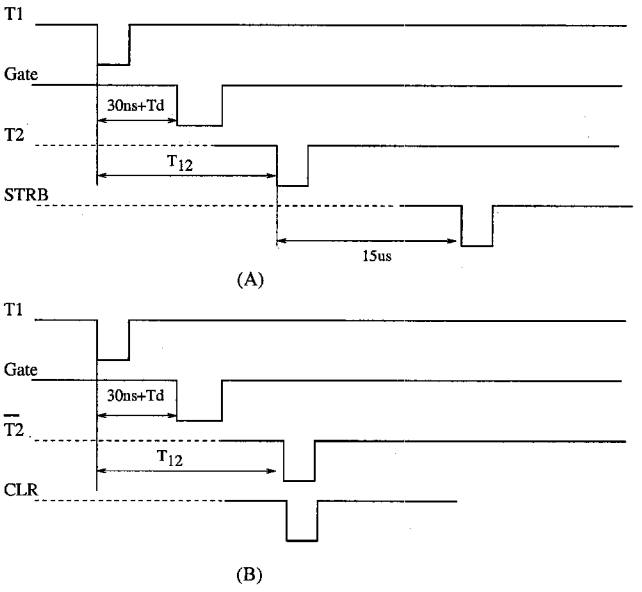

Fig. 8. ADC local trigger timing diagram. (A): $T1$ with $T2$. Gate and strobe to FSCC are generated, or event is accepted. (B) $T1$ with $\bar{T}2$. Gate and clear are generated or event is rejected.

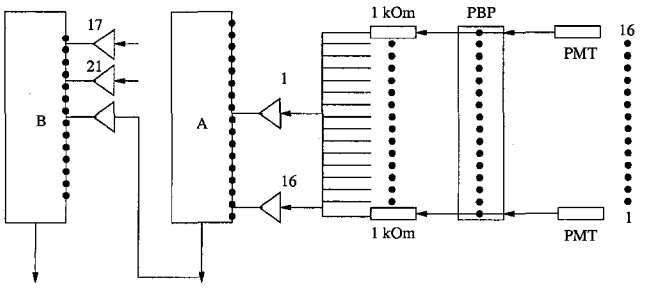

Fig. 9. A scheme of Photon 3 trigger.

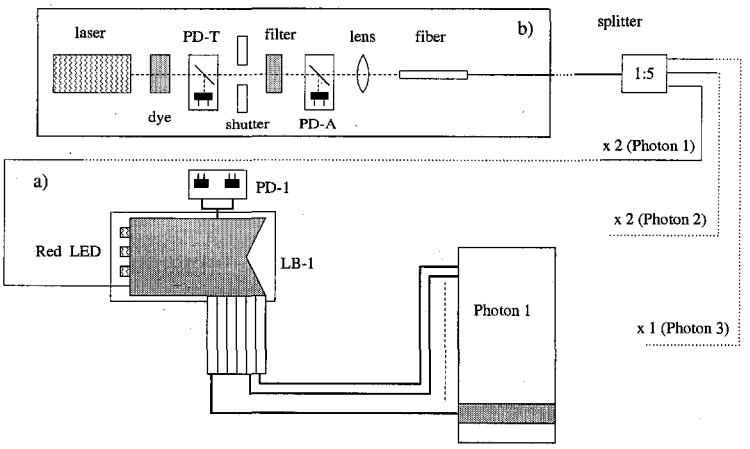

Fig. 10. A scheme of the monitoring system.

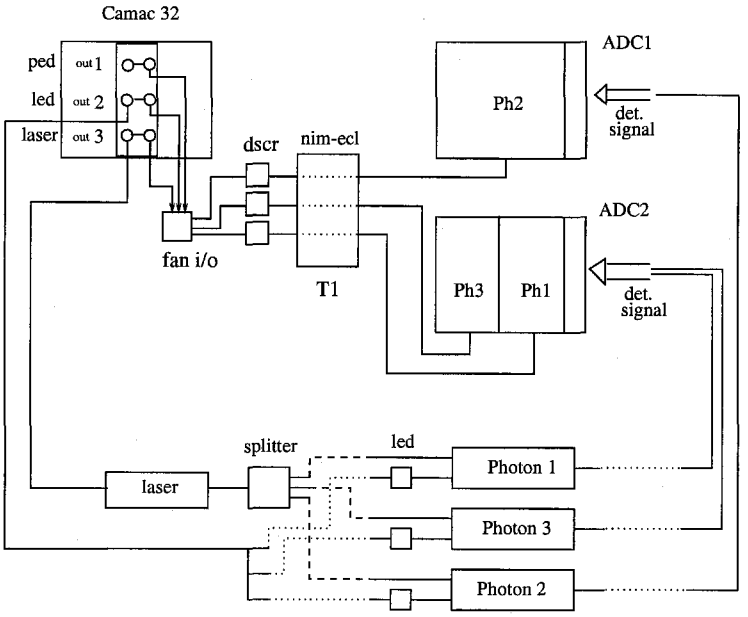

Fig. 11. A sketch of the readout electronics.

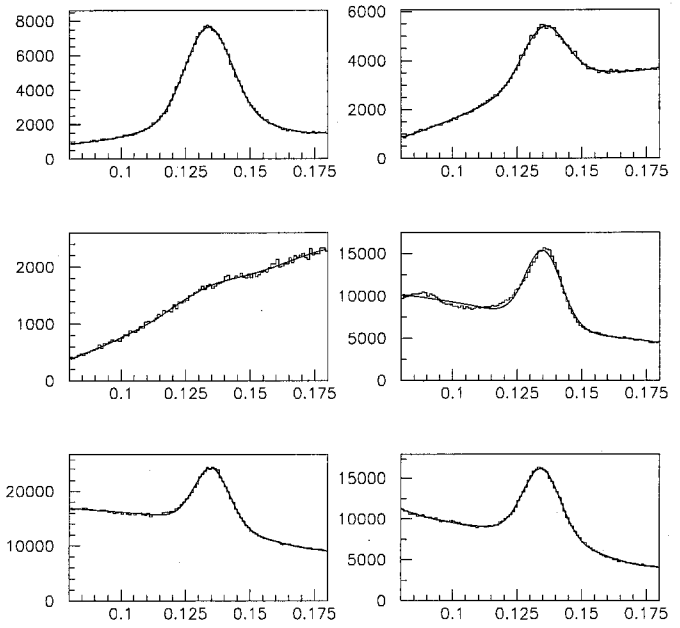

Fig. 12. The effective mass distribution for the $\gamma\gamma$ system, for isolated gammas with $E_\gamma > 2$ GeV. Pictures from left to right, upper raw: both gammas hit Photon 1 - "11", one gamma hit Photon 1 and second hit Photon 2 -"12", middle raw: first gamma hit Photon 1 and second hit Photon 3 -"13", both gammas hit Photon 2 -"22", bottom raw: first gamma hit Photon 2 and second hit Photon 3, both gammas hit Photon 3 "33". Fits presented in Table 4.

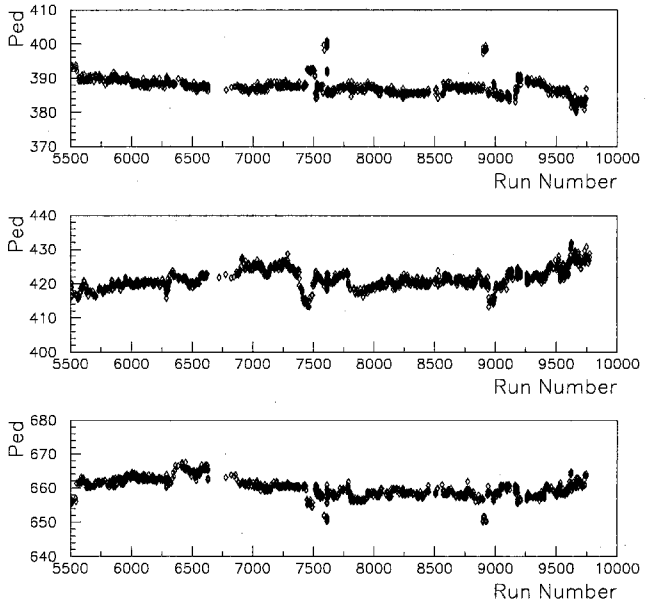

Fig. 13. ADC pedestal behavior for three typical counters (one from each of Photon detectors) during data taking.

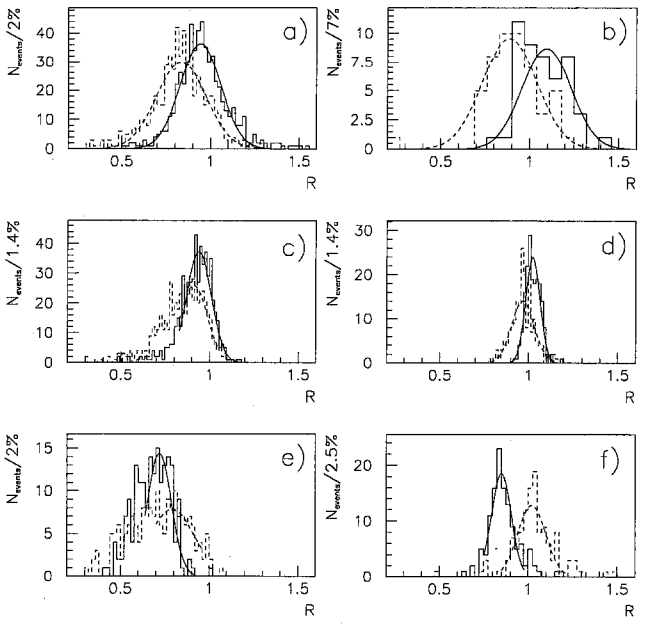

Fig. 14. Distributions on R_{corr} (solid histogram) and on R_{uncorr} (dashed histogram) for small (a) and big (b) blocks of the Photon 1, for small (c) and big (d) blocks of the Photon 2, and for ordinary (e) and radiation hard (f) blocks of the Photon 3. The Gaussian fits are shown by curves

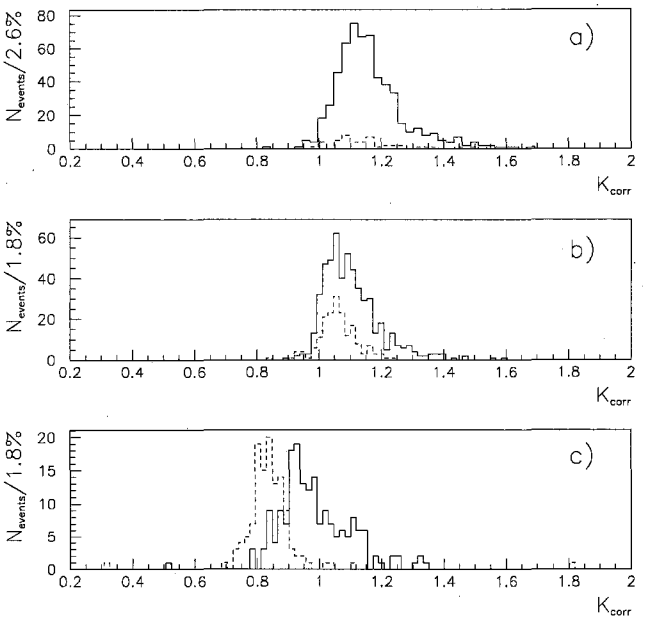

Fig. 15. Distribution on K_{corr} - for small (dashed histogram) and big blocks (solid histogram) of the Photon 1 (a), for small (dashed histogram) and big blocks (solid histogram) of the Photon 2 (b), and for ordinary (dashed histogram) and radiation hard (solid histogram) of the Photon 3 (c)

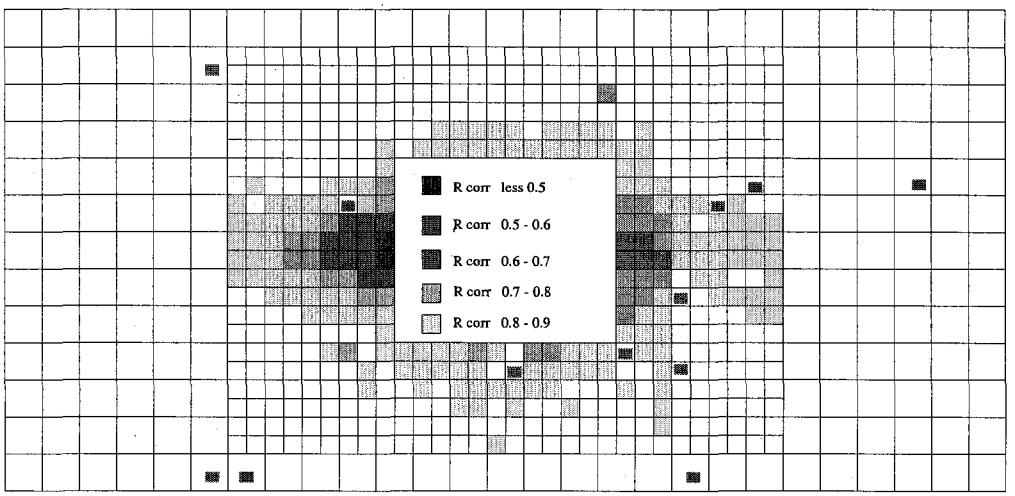

Fig. 16. The graphical mapping of R_{corr} for some Photon 2 radiation damaged counters. Counters with the same value of R_{corr} are shown with the same color. Small hatched rectangles mark the blocks with replaced channels which were excluded from the analysis.

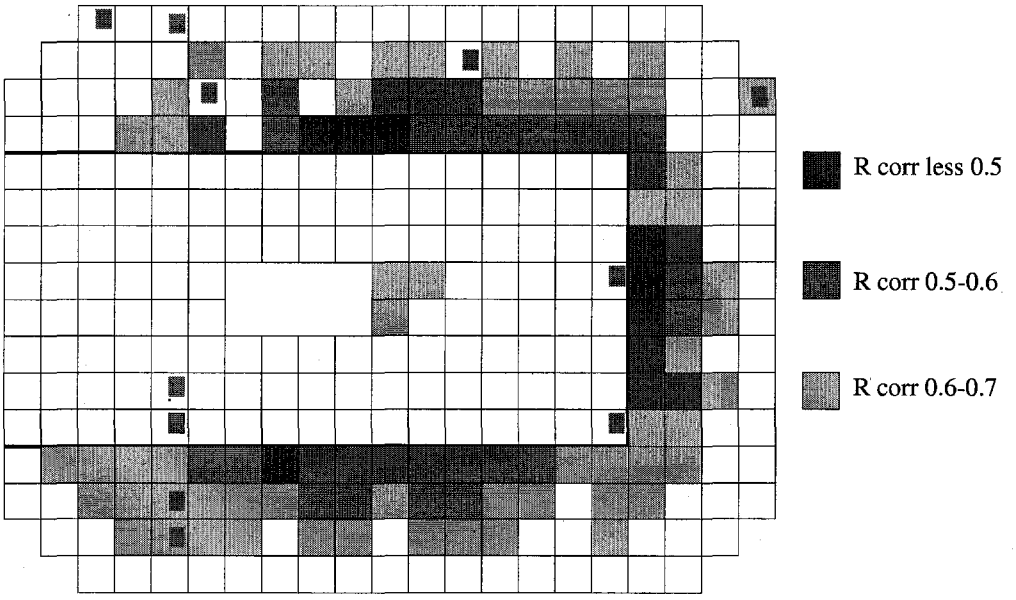

Fig. 17. The graphical mapping of R_{corr} for some Photon 3 radiation damaged counters. Counters with the same value of R_{corr} are shown with the same color. Small hatched rectangles mark the blocks with replaced channels which were excluded from the analysis.

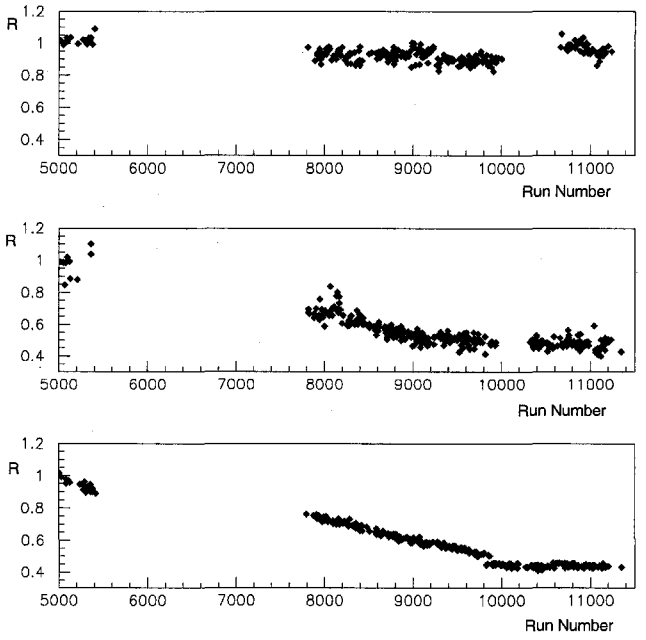

Fig. 18. Long-term variation of R_{corr} in time for typical counters from Photon 1 (top), for the damaged counters from Photon 2 (middle) and for the damaged counters from Photon 3 (bottom).

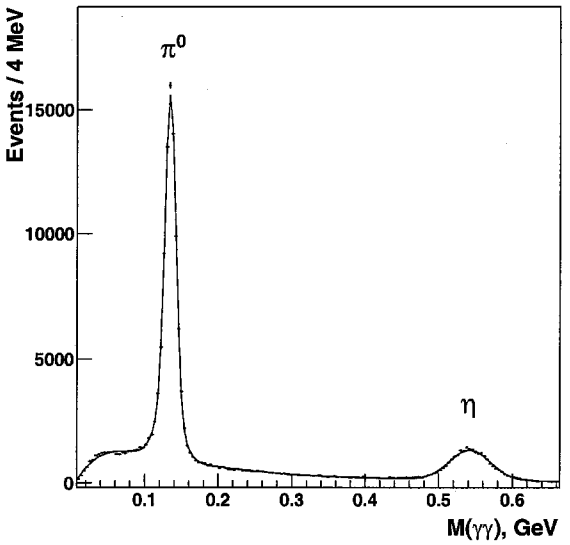

Fig. 19. The effective mass distribution for the $\gamma\gamma$ system (π^- beam, exclusive trigger, $E_\gamma > 2$ GeV, $N_\gamma = 2$, $E_{\gamma\gamma} > 10$ GeV). Mass resolution $\sigma(M)/M$ is 6% for the π^0, and 5% for the η.

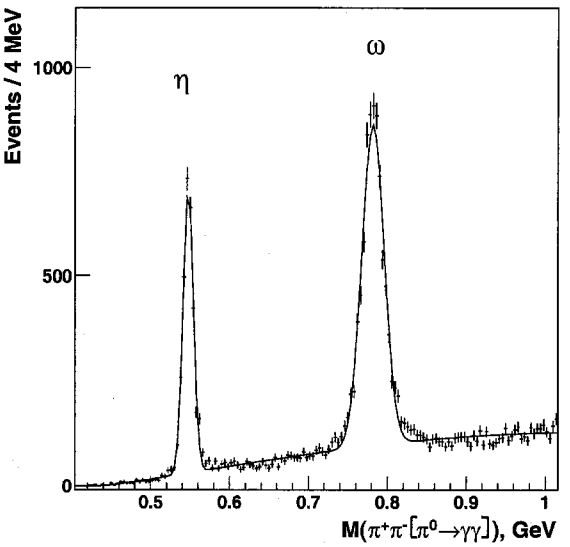

Fig. 20. The effective mass distribution for the $\pi^+\pi^-\pi^0$ system (Σ^- beam, exclusive trigger, $E_\gamma > 2$ GeV, $N_\gamma = 2$, $E_{\pi^0} > 10$ GeV). The mass resolution $\sigma(M)/M$ is 1.2% for the η and 1.8% for the ω.

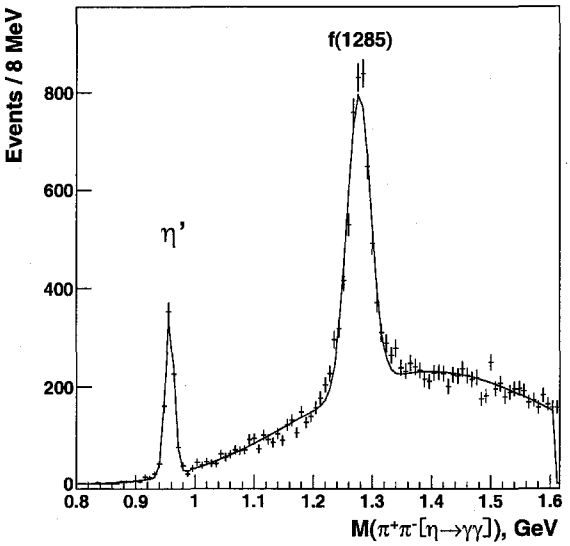

Fig. 21. The effective mass distribution for the $\pi^+\pi^-\eta$ system (Exclusive trigger, $E_\gamma > 2$ GeV, $N_\gamma = 2$, $E_\eta > 10$ GeV). The mass resolution $\sigma(M)/M$ is 0.8% for the η', and 1.35% for the f respectively.

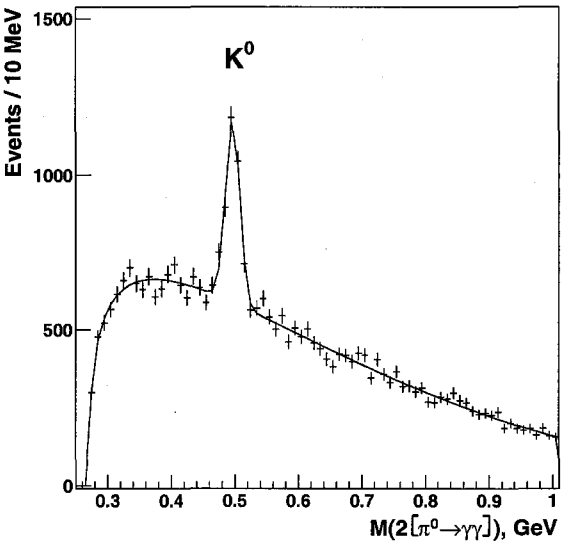

Fig. 22. The effective mass distribution for the $2\pi^0$ system (Σ^- beam, exclusive trigger, $E_\gamma > 4$ GeV, $N_{\pi^0} \leq 4$, $E_{\pi^0} > 30$ GeV). The mass resolution $\sigma(M)/M$ for the K^0 is 2.2%

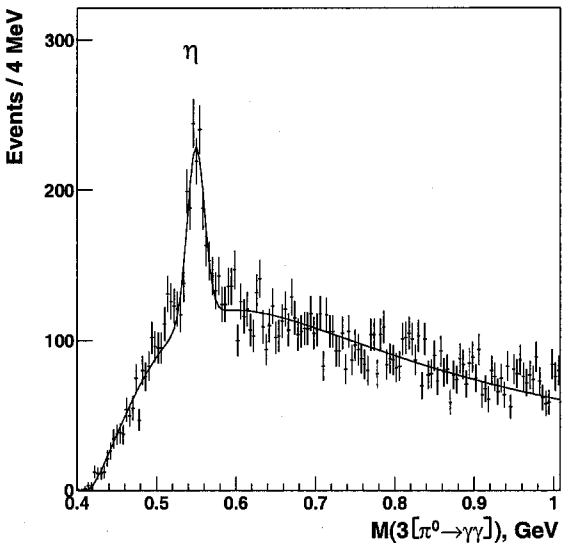

Fig. 23. The effective mass distribution for the $3\pi^0$ system (Σ^- beam, exclusive trigger, $E_\gamma > 5$ GeV, $N_\gamma = 6$, $E_{\pi^0} > 20$ GeV). The mass resolutions $\sigma(M)/M$ for the η is 1.9%.

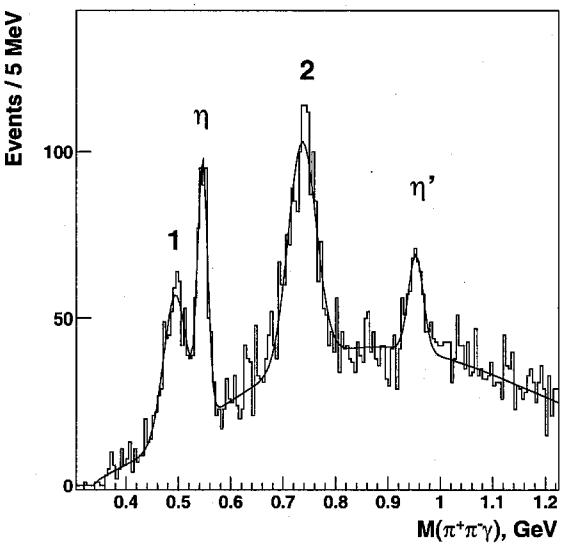

Fig. 24. The effective mass distribution for the $\pi^+\pi^-\gamma$ system (Σ^- beam, exclusive trigger). 1 is "false" peak from decay process $\eta \to \pi^+\pi^-\pi^0$ with one γ missing. 2 is "false" peak from decay process $\omega \to \pi^+\pi^-\pi^0$ with one γ missing. False peaks are shifted to lower values of mass.

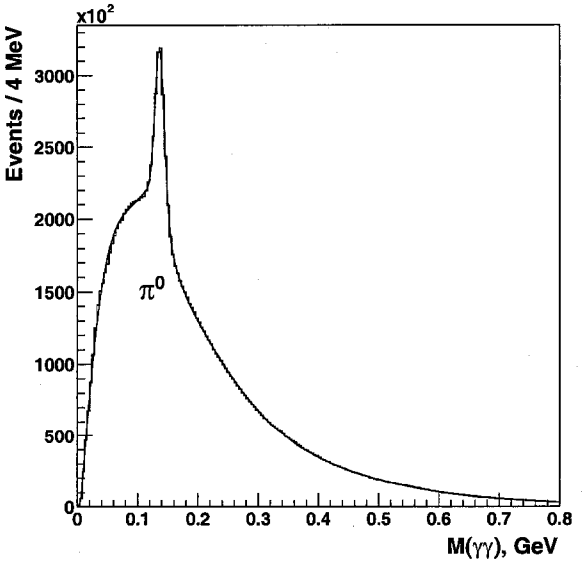

Fig. 25. The effective mass distribution for the $\gamma\gamma$ system (charm trigger, $N_\gamma \leq 10$, $E_\gamma > 2$ GeV, $E_{\gamma\gamma} > 10$ GeV). The π^0 mass resolution $\sigma(M)/M$ is 6%.

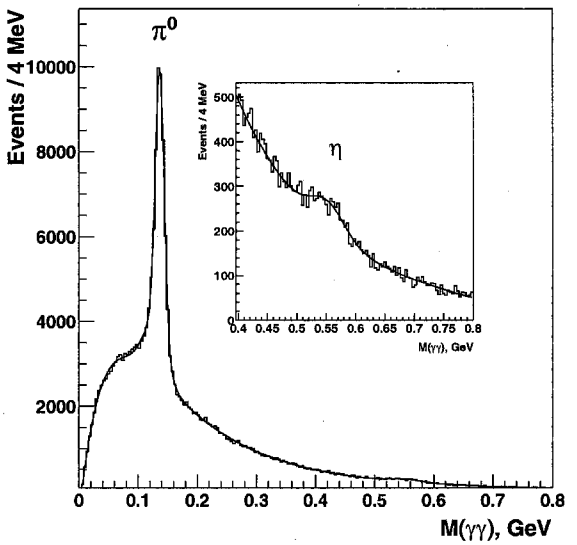

Fig. 26. The effective mass distribution for the $\gamma\gamma$ system (charm trigger, $N_\gamma = 2$, $E_\gamma > 2$ GeV, $E_{\gamma\gamma} > 10$ GeV). The π^0 mass resolution $\sigma(M)/M$ is 7%, and the η mass resolution $\sigma(M)/M$ is 5%.

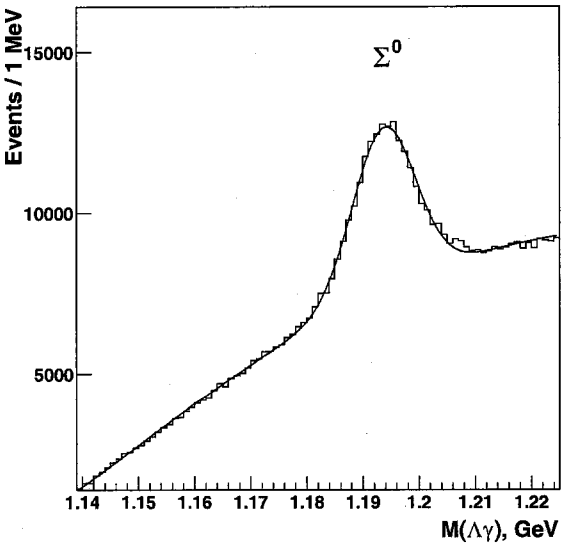

Fig. 27. The effective mass distribution for the $\Lambda\gamma$ system (charm trigger with $E_\gamma > 6$ GeV). The Σ^0 mass resolution $\sigma(M)/M$ is 0.46%.

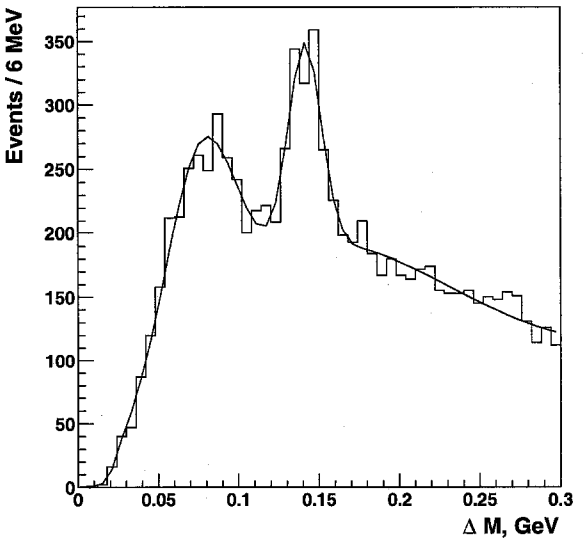

Fig. 28. The $\Delta M_\gamma = M(D^0\gamma) - M(D^0)$ (charm trigger with $E_\gamma > 5$ GeV).

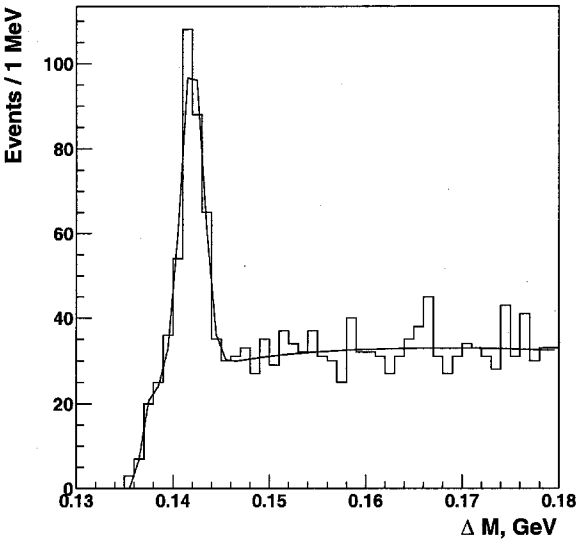

Fig. 29. The $\Delta M_{\pi}^{0} = M(D^{0}\pi^{0}) - M(D^{0})$ distribution (Charm trigger with $E_{\gamma 1,2} > 3$ GeV).